LITHOS 486–487 (2024) 107777

Contents lists available at ScienceDirect

LITHOS

journal homepage: www.elsevier.com/locate/lithos

Unusual spinel in the "Verde Prato" serpentinized peridotite

Giancarlo Capitani [a,*], Roberto Compagnoni [b,c], Roberto Cossio [b,c], Linda Pastero [b], Roberto Conconi [a], Marcello Mellini [c]

[a] Dept. of Earth and Environmental Sciences (DISAT), University of Milano Bicocca, 20126 Milano, Italy
[b] Dept. of Earth Sciences, University of Turin, Via Valperga Caluso 35, 10125 Torino, Italy
[c] "G. Scansetti" Interdepartmental Centre for Studies on Asbestos and Other Toxic Particulates, University of Turin, Via Pietro Giuria 7, 10125 Torino, Italy

ARTICLE INFO

Keywords:
Serpentinization
Spinel
Hydrothermal alteration
Al-lizardite
Phase map
TEM-EDS

ABSTRACT

A petrographic study of "*Verde Prato*" (trade name of an ophiolitic serpentinised peridotite quarried in Tuscany) revealed, next to a relict Cr-spinel, another opaque ore mineral apparently containing ca.17 wt% SiO_2. In order to unveil the origin of this anomalous composition, detailed SEM-EDS, μ-Raman spectroscopy and X-ray μ-diffraction investigations were undertaken, which provided useful but somehow contrasting indications. Therefore, in order to definitely unveil the nature of the unusual opaque mineral, a specific TEM study was undertaken. This showed the presence of submicroscopic euhedral Mn-Cr-Fe-spinels in a matrix of a 7 Å layer-silicate (Al-lizardite). Interesting, all the submicroscopic spinel grains were found to share the same crystallographic orientation, suggesting an origin from a single, larger, former crystal. This unusual type of alteration of the mantle spinel probably occurred on the ocean floor during the pervasive polyphase process of hydrothermal peridotite serpentinization. Overall, by mapping the different serpentinite microstructures and compositions, a polyphase serpentinization history consisting of at least eight different cycles has been suggested. Moreover, the spinel composition indicates that the alteration was accompanied by Mn-metasomatism, made possible by the close proximity of Mn-rich hydrothermal vents, such as "black smokers".

1. Introduction

Complex geological processes lead to the formation of valuable natural resources such as economic minerals and ornamental stones and the study of natural resources may convey important insights into the geological processes that originated them. In this context, Coli et al., (2023) undertook a study of an ornamental stone known with the trade name of "*Verde Prato*" (*Green stone from Prato*), an ophiolitic serpentinised peridotite, quarried in Tuscany. These authors found that the original mantle protolith is partially preserved within the serpentinite body, showing, locally, vestiges of sub-continental mantle deformation that recorded the early stages of lithosphere extension that opened the Ligurian Tethys. These peridotitic minerals then underwent bulk serpentinization with a late formation of chrysotile and lizardite veins, with the former cross-cutting the latter. Very rare antigorite veins were also detected, although in this case the relationships with the other veins were less obvious. However, while the main petrographic and microstructural features led to the scenario depicted above, minor evidences remain unexplained, such as the presence of an opaque phase with unusual chemical composition and fabric. Peculiarities were the isotropic habit of the opaque ores, their intimate association with lizardite derived from former orthopyroxene, and especially the chemical composition characterized by systematic high silica content (ca.17 wt% SiO_2), unlikely for a member of the spinel family. These oddities led to a detailed study, mostly aimed at explaining the chemical anomaly, using polarizing microscopy, scanning electron microscopy (SEM), energy dispersive spectroscopy (EDS), transmission electron microscopy (TEM), μ-Raman spectroscopy and μ-area X-ray powder diffraction (μ-XRPD).

In this paper, we report the results of the aforementioned analyses, which sometimes lead to conflicting interpretations. However, these conflicts were eventually reconciled by delving into the investigation at the nanometric scale, ultimately explaining the spinel anomaly. As a corollary, this in depth study revealed that the serpentinization event was polyphasic, made of at least eight distinct cycles.

* Corresponding author.
E-mail address: giancarlo.capitani@unimib.it (G. Capitani).

https://doi.org/10.1016/j.lithos.2024.107777
Received 22 May 2024; Received in revised form 27 July 2024; Accepted 25 August 2024
Available online 28 August 2024

2. Materials and methods

The "*Verde Prato*" samples come from the Monteferrato ophiolitic body, which is part of the Monte Morello Unit. This is the lowermost tectonic slice of the Ligurian Units that derived from the floor of the Mesozoic Ligurian Ocean and overthrust the Tuscan Nappe during the Apennine orogeny (Coli et al., 2023, with references therein). The Monteferrato Ophiolite consists of a main body of serpentinized peridotite, intruded by gabbro and basalt dykes and covered by massive and pillowed basalts, capped by radiolarian chert (CARG, 2012). Samples were collected from the now disused, historical and best-exposed Guarino quarry (coordinates 43°55′44"N, 11°04′23″E), located in the NW part of the Monteferrato Ophiolite (Coli et al., 2023). A number of specimens were sampled from the best-preserved massive and non-foliated serpentinized peridotite blocks, piled up at the quarry yard. From the most representative samples, 12 polished thin sections, labelled FIB1 to 12, were prepared and studied in detail.

Chemical data were acquired with a SEM (JEOL JSM-IT300LV) equipped with an EDS Oxford Instruments X-act silicon drift detector. Operating conditions were: E = 15 keV, working distance = 10 mm, magnification = 50× (2.55 * 1.9 mm scanned area), 1024 × 768 pixels (res = 2.5 μm), probe current = 5 nA, process time = 1 μs (10^5 counts per second (CPS) with a dead time of 30 %), SmartMap dwell time = 10 ms. Phase maps were obtained with AZtec AutoPhaseMap (Oxford Instruments) from quantitative X-ray maps of individual element calculated with AZtec QuantMap (Oxford Instruments). Sum spectra extracted for each main phase (Lz: lizardite, Spl: spinel, Mag: magnetite) were quantitatively corrected using the ZAF procedure. Atom concentrations per formula unit (a.p.f.u) were obtained by means of Lanari functions (Lanari et al., 2014).

The TEM investigation was performed by a Jeol JEM 2100P at the Platform of Microscopy of the University of Milano Bicocca (PMiB). The instrument is equipped with an Oxford EDS system for elemental analysis and a Gatan Rio CMOS camera for image acquisition, and can operate at an accelerating voltage between 80 and 200 kV (we used 200 kV), either in conventional or scanning (STEM) mode. Images were taken in Bright Field (BF) and High Resolution (HR) modes at magnifications between 15 and 300 kX. EDS analyses were quantified using standards of known composition and corrected for absorption (Conconi et al., 2023). Samples were prepared by ion milling 3 mm wide disks, selected on a double polished petrographic thin section, using a Gatan PIPS-II cool instrument at the PMiB. Before removing the disk and ion milling, a 3 mm wide Cu-ring with an internal hole of 1 mm was glued on the area of interest. TEM-mounts were coated with 5 nm of carbon to avoid electrostatic charging during observations.

3. Results

3.1. Petrography

Thin sections confirmed that the rock is lacking anisotropy even at the microscale. The serpentinization process mainly produced pseudomorphous reactions that preserved the details of the peridotite microstructure, allowing the original mantle mineralogy to be identified.

Pseudomorphs after olivine consist of fine-grained lizardite aggregates characterized by dusty appearance because of very fine-grained dispersion of magnetite grains (Fig. 1 and 2A). Pseudomorphs after orthopyroxene consist of clear lizardite lacking the typical dispersion of fine magnetite grains (Figs. 1 and 2A). In all the serpentinite samples, ubiquitous thin veins of "slip" chrysotile and rare antigorite veins were observed. For a more exhausting petrographic description of "*Verde Prato*" refer to Coli et al. (2023).

Three types of spinels have been distinguished on the base of microstructure and/or composition: *i)* a rare relict mantle spinel (*Spl1*), *ii)* a ubiquitous opaque spinel (*Spl2*), and *iii)* a late magnetite spinel (*Spl3*).

Spl1, identified and analysed in sample FIB9, is a dark reddish-brown spinel with corroded habit, rimmed along contours and fractures by a very thin discontinuous rim of magnetite (*Spl3*) (Fig. 1A). Its composition, determined by Coli et al. (2023), indicates "picotite", which plots in the Cr-Al trend of ophiolites and oceanic peridotites (as defined by Barnes and Roeder, 2001), and in the field of abyssal peridotites (Bédard et al., 2009). According to the experimental data of Hellebrand et al. (2001) its chrome number (Cr# = 0.33–0.32) indicates a depleted harzburgite protolith (Coli et al., 2023).

The ubiquitous opaque *Spl2* consists of opaque shards with strongly corroded habit (Fig. 1B and 2), which are intimately associated or intergrown with clear lizardite patches. In statically serpentinized ultramafics, these clear lizardite domains are considered pseudomorphous after former orthopyroxene (e.g., Bédard et al., 2009). Consequently, the clear lizardite + *Spl2* microstructure can be interpreted as former spinel-orthopyroxene intergrowths derived from static breakdown of a precursor garnet, occurred in the mantle during decompression from the garnet- to spinel-peridotite facies conditions (e.g., Guarnieri et al., 2012; O'Neill, 1981; Shimizu et al., 2008).

Spl3 is magnetite, most likely a by-product of the olivine serpentinization process. Magnetite occurs as either small isometric grains embedded in the lizardite groundmass derived from former olivine (Fig. 1B and 2) or thin discontinuous coronas rimming the contours of *Spl1* spinels or their fractures (Fig. 1A).

For the detailed study of the ubiquitous *Spl2* and the surrounding serpentinite, a site was selected (Fig. 2A), where elongated and corroded

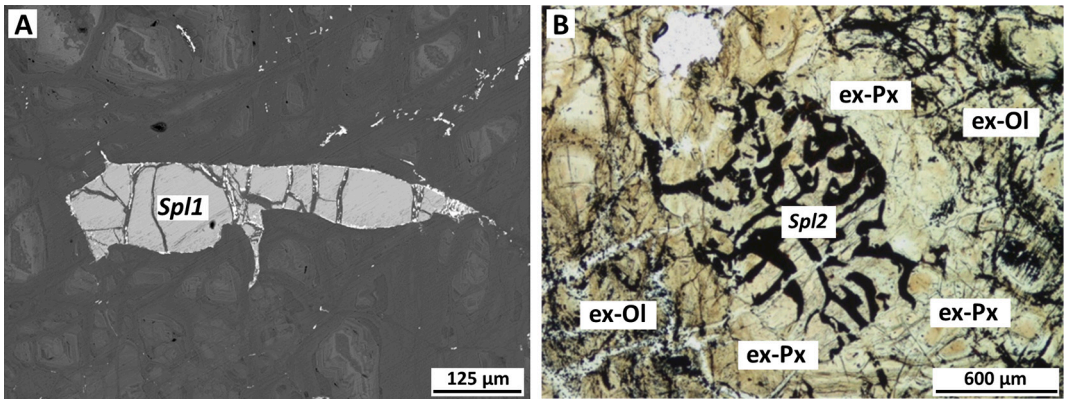

Fig. 1. A) Back-scattered electron (BSE) image of *Spl1* showing a corroded relic of the original dark-reddish brown spinel ("picotite") included in a fine-grained lizardite matrix. The white dots, occurring as rims of "picotite" or thin worms, are magnetite. **B)** Plane polarized light micrograph of *Spl2* showing roundish intergrowth of corroded opaque spinel (*Spl2*) with clear lizardite after former orthopyroxene (ex-Px), surrounded by dusty serpentine crowded by magnetite after former forsterite (ex-Ol) (Sample FIB1). (For interpretation of the references to colour in this figure legend, the reader is referred to the web version of this article.)

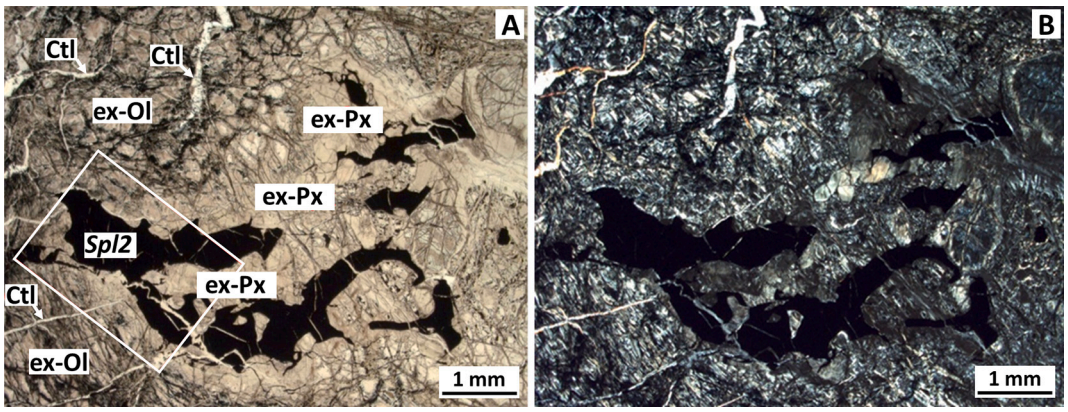

Fig. 2. A) Plane polarized light micrograph of representative site of corroded opaque shards of *Spl2* embedded in a fine-grained aggregate of clear lizardite, pseudomorphous after former pyroxene (ex-Px), and surrounded by darker aggregates of lizardite and very fine-grained magnetite after former olivine (ex-Ol). The thin irregular white veins consist of "slip-type" chrysotile (Ctl). The white box delimits the SEM-BSE image and phase map of Fig. 3. **B**) Crossed polarized light micrograph of A (Sample FIB2 A).

opaque shards, included in a clear lizardite domain after orthopyroxene, show a rough preferred orientation. Previous SEM-EDS analyses of *Spl2* showed a bulk chemistry characterized by too high silica content (SiO_2 ≈ 17 wt%), but μ-XRPD and μ-Raman studies were unable to explain its anomalous chemical composition. In addition, having noticed the unexpected compositions of lizardites adjacent to *Spl2* (Fig. 3), a representative serpentinite portion, where the microstructural relationships among serpentine generations were particularly clear, was analysed by SEM-EDS (Fig. 4).

3.2. SEM-EDS results

SEM-EDS analyses were carried out on sample FIB2A, which contains the opaque *Spl2* and the associated clear lizardite (Fig. 3) and on sample FIB1, where the microstructural relationships among serpentines are evident (Fig. 4).

The phase map of Fig. 3, which corresponds to the area included in the white box of Fig. 2A, shows four domains with different compositions highlighted by false colours. These correspond to the opaque *Spl2* (yellow), two adjancent domanins of clear lizardites (*Lz1,* purple; *Lz2*, green) surrounding *Spl2*, and magnetite (whitish pink), respectively. The mean compositions of *Spl2, Lz1* and *Lz2* are reported in Tables 1 and 2.

One hundred fifty SEM-EDS spot analyses were randomly selected in the yellow portion of the phase map of Fig. 3. Each spectrum contains 300,000 counts with a standard deviation of about 3 % for major elements (Table 1). SEM-EDS analyses were relatively homogeneous all over the *Spl2* domain, but showed unexpected anomalous results. In fact,

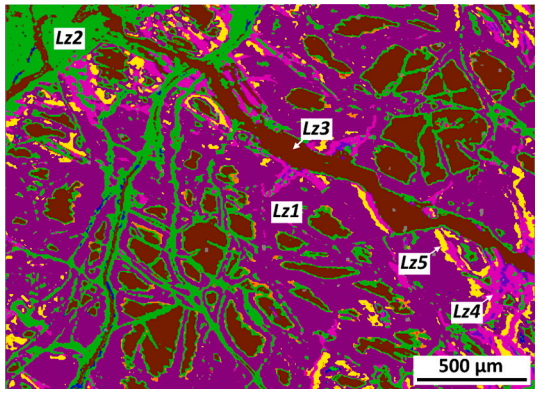

Fig. 4. Phase map of a representative serpentinite portion of sample FIB1. The chronological order of the different lizardite generations is evident. Eight homogeneous lizardite domains are highlighted with colours: 1 = dark purple, 2 = green, 3 = brown, 4 = light purple, 5 = yellow, 6 = orange, 7 = azure, 8 = blue. The analyses of the five most significant domains are reported in Table 3, which correspond to ca. 96 % of the whole phase map. (For interpretation of the references to colour in this figure legend, the reader is referred to the web version of this article.)

alongside elements (such as Mg, Cr, Fe, Mn, Al and Ti) compatible with the spinel chemistry (e.g., Bosi et al., 2019), the SiO_2 content (16.97 ± 0.59 wt%) resulted too high, being usually below 1 wt% for this mineral

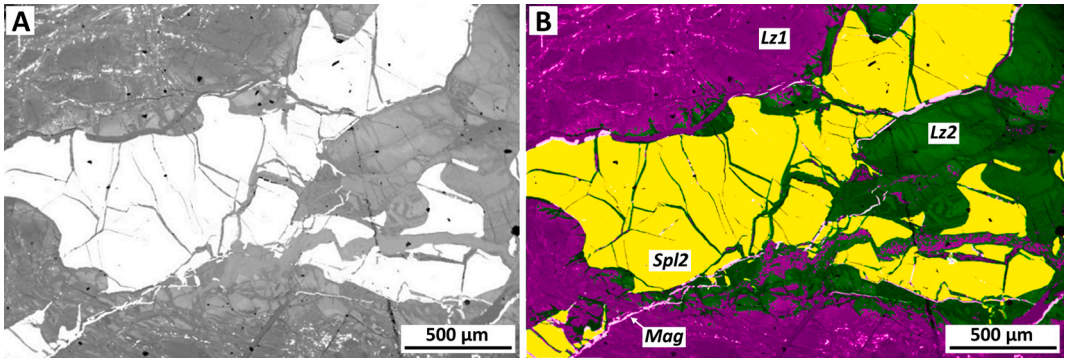

Fig. 3. A) BSE image of the opaque shards of *Spl2* included in the white box of Fig. 2A. The *Spl2* opaque shards (white) are surrounded by fine grained aggregate of clear lizardite (different shadows of grey) and very minor magnetite (thin white alignments and dots). **B**) Phase map, superimposed on the BSE image, that is highlighting four different compositions: the opaque *Spl2* (yellow), two types of lizardite (*Lz1,* purple; *Lz2*, green), and magnetite (*Mag*, whitish pink) (sample FIB2A). (For interpretation of the references to colour in this figure legend, the reader is referred to the web version of this article.)

Table 1
Mean chemical composition and standard deviation of 150 spot analyses from the opaque shards of *Spl2* (yellow colour in Fig. 3B), sample FIB2A, compared to mean composition and Std. Dev. of 450 spot analyses along profiles across five opaque grains of sample FIB2B (Fig. S1). Minor oxides (Ni, Ca, Zn) whose Std. Dev. was higher than, or similar to, the mean value, were not considered.

	Sample FIB2A		Sample FIB2B	
Oxide	Mean wt%	Std. Dev.	Mean wt%	Std. Dev.
FeO	25.11	2.17	23.05	2.77
Cr_2O_3	23.73	1.34	21.13	0.94
MgO	18.53	0.61	21.64	1.42
MnO	9.45	0.73	8.15	0.59
TiO_2	0.69	0.48	1.11	0.52
SiO_2	16.97	0.59	18.29	1.28
Al_2O_3	4.36	0.37	5.63	0.45
Tot.	98.75		99.25	

Table 2
Average compositions of the two lizardites shown in Fig. 3 with purple (*Lz1*) and green (*Lz2*) colours, respectively. Atoms per formula unit (a.p.f.u) calculated on the base of five oxygens (Sample FIB2A).

Oxide (wt%)	*Lz1*	*Lz2*
SiO_2	46.80	45.17
Al_2O_3	1.27	4.34
FeO	6.56	6.12
MnO	0.08	0.17
MgO	44.56	42.04
NiO	0.50	0.36
Cr_2O_3	0.28	1.84
Total	100.05	100.04
a.p.f.u.	***Lz1***	***Lz2***
Si_T	1.943	1.877
Al_T	0.057	0.123
Fe_M	0.228	0.213
Mg_M	2.759	2.605
Cr_M	0.009	0.060
Ni_M	0.017	0.012
Al_M	0.005	0.090
Mn_M	0.003	0.006
X_{Fe}	0.076	0.074
X_{Mg}	0.916	0.901
$\sum_M$	3.021	2.986

family. Furthermore, the MnO content (9.45 ± 0.73 wt%) is approximately an order of magnitude higher than what expected for a mantle spinel. To verify whether this unusual chemistry was present also in other *Spl2* spinels, four corroded opaque grains with different habits from sample FIB2B were analysed along representative cross profiles (see supplementary material, Fig. S1). The results of 450 spot analyses (Table 1) gave average values of SiO_2 (18.28 ± 1.28 wt%) and MnO (8.15 ± 0.59 wt%), which match those of sample FIB2A, implying that both samples were affected by the same alteration process. The above observations may be explained by a submicroscopic and intimate association of spinel with silicate, such as lizardite or a similar phyllosilicate, as elsewhere observed by Mellini et al. (2005).

The phase map of Fig. 3 also shows that two distinct lizardites, highlighted with purple (*Lz1*) and green (*Lz2*) colours, occur in the serpentinite matrix surrounding *Spl2*. As evident from Table 2, both lizardites have similar high Fe content (FeO > 6 wt%), but variable Al_2O_3 content, lower in *Lz1* (1.27 wt%) with respect to *Lz2* (4.34 wt%). Furthermore, both lizardites have low but significant NiO and Cr_2O_3 contents.

To test whether these features were common all over the serpentinite, even far from the studied *Spl2* spinel site, a homogeneous rock portion of sample FIB1 was selected, lacking pseudomorphs after mantle minerals but showing several lizardite generations with obvious microstructural and chronologic relationships.

Fig. 4 is a phase map of the analysed serpentinite. Here, at least eight domains, characterized by different lizardite compositions, can be recognized. The composition of each domain is the average of ca. 60 randomly selected spot analyses, with Mn, Ni, K, Ca and Ti not considered because below detection limit. The mean values of the five most representative lizardite domains, which correspond to 96 % of the total mapped area, are reported in Table 3 with the relative standard deviations.

Based on geometric relationships among the different serpentine domains in Fig. 4, the serpentinization process appears to have occurred in at least eight stages, each characterized by a distinct lizardite chemical composition. Domains labelled *Lz1*, *Lz2* and *Lz3* (with area covering 85 % of the serpentinite) developed in chronological order, forming lizardites with progressively decreasing Al, from 7.84 to 3.62 wt%, and Fe, from 7.44 to 3.57 wt% (Table 3). On the contrary, domains *Liz 4* and *Liz 5* (which correspond to a further 11 % of the analysed area), show increasing Al from 8.17 to 9.38 wt% and Fe from 4.79 to 8.48 wt%. Furthermore, the five lizardite generations have average Cr content of 1.23 wt%.

3.3. μ-Raman and μ-XRPD results

Aiming at solving the oddity evidenced by the *Spl2* opaque shards, we first attempted μ-Raman spectrometry, whose laser beam has a diameter of only one micron, and then μ-XRPD, examining areas as low as 2 μm^2.

Raman results indicate that the *Spl2* is a chromite-rich spinel with very low Al content. However, all Raman spectra, carried out on a great number of opaque *Spl2* shards from samples FIB2A and FIB2B, never showed additional peaks referable to other minerals, in particular to silicate phases (*Appendix A*). A possible explanation of this absence could be the overprinting effect of the strong spinel spectrum that is masking the weaker silicate Raman signal. The μ-XRPD results confirmed that Mn occurs in a spinel with the manganochromite composition, and confirmed that the silicate phase included in the opaque shards might be a 7 Å layer-silicate similar to lizardite (*Appendix B*). However, since both μ-Raman and μ-XRPD analyses did not give definitive results, in order to get more insight into the apparently complex and reluctant nature of the *Spl2* opaque, we undertook a TEM investigation.

3.4. Transmission Electron Microscopy Results

The TEM images of the opaque *Spl2* show euhedral spinels surrounded by a layer-silicate envelope. Spinel crystals have orthogonal contours; their size ranges between 0.2 and 2 μm, typically being 0.3–0.4 μm. The layer-silicate is 0.1 to 0.5 μm thick (Fig. 5A and B). All spinel crystals entering the larger field limiting aperture (120 μm), share a common orientation, apart some minor, usual mosaicity, suggesting inheritance from a former single crystal, now disrupted.

The relative amounts of spinel and layer-silicate were estimated from representative TEM EDS maps (Figs. 5, 6, S2, S3 and similar other images not reported). Here, the pixels assigned to the two phases, once normalized to 100 %, indicate modal percentages of 45 vs. 55 % for spinel and layer-silicate, respectively. Even considering the possible error due to the very small areas analysed by TEM, we conclude that, modally, the layer-silicate slightly prevails over spinel.

TEM-EDS chemical analyses were based on standards and corrected for absorption (Conconi et al., 2023). Table 4 reports average TEM-EDS compositions of five spot analyses (image of the analysed area with the relative TEM-EDS spectra is reported in Fig. S4). A final formula was calculated omitting minor elements (i.e., those with mean value lower than the first decimal, namely Mg, Al, Si, Ca, Ni, Zn). This indicates a spinel composition mainly consisting of Fe, Cr and Mn, namely:

$(Mn_{0.54}\ Fe^{2+}_{0.46})_{\Sigma=1.00}\ (Cr_{1.15}\ Fe^{3+}_{0.85})_{\Sigma=2.00}\ O_{4.00}$

i.e., a solid solution of manganochromite and chromemagnetite in approximately equal proportions.

Table 3
Mean chemical composition (standard deviation every second column), modal percentage, and atoms per formula unit of lizardites representative of the 5 most significant serpentine domains, corresponding to 96 % of the analysed area. *Liz1* to *Liz5* are numbered in chronological order, and colours (in brackets) refer to Fig. 4.

Oxides (wt%)	*Lz1* (red)		*Lz2* (green)		*Lz3* (brown)		*Lz4* (purple)		*Lz5* (yellow)	
SiO_2	43.37	0.35	45.08	0.63	47.65	0.59	43.46	0.36	42.11	0.39
Al_2O_3	7.84	0.39	5.93	0.52	3.62	0.53	8.17	0.26	9.38	0.33
FeO	7.44	0.37	5.87	0.91	3.57	0.57	4.79	0.41	8.48	0.53
MgO	39.29	0.22	41.18	0.66	43.98	0.90	41.60	0.47	37.97	0.37
Cr_2O_3	1.33	0.15	1.35	0.42	0.68	0.30	1.40	0.13	1.39	0.23
Total	99.30		99.41		99.53		99.40		99.32	
Modal %	45.7		20.2		18.9		7.2		4.0	(Total = 96.0)

Atoms per formula unit (calculated on the base of 5 oxygens)					
Si_T	1.810	1.866	1.944	1.793	1.767
Al_T	0.190	0.134	0.056	0.207	0.233
Al_{Tot}	0.386	0.289	0.174	0.397	0.464
Al_M	0.196	0.155	0.118	0.190	0.231
Fe_M	0.260	0.203	0.122	0.165	0.298
Mg_M	2.445	2.541	2.676	2.560	2.375
Cr_M	0.044	0.044	0.022	0.046	0.046
X_{Fe}	0.094	0.073	0.043	0.060	0.109
X_{Mg}	0.890	0.911	0.949	0.924	0.874

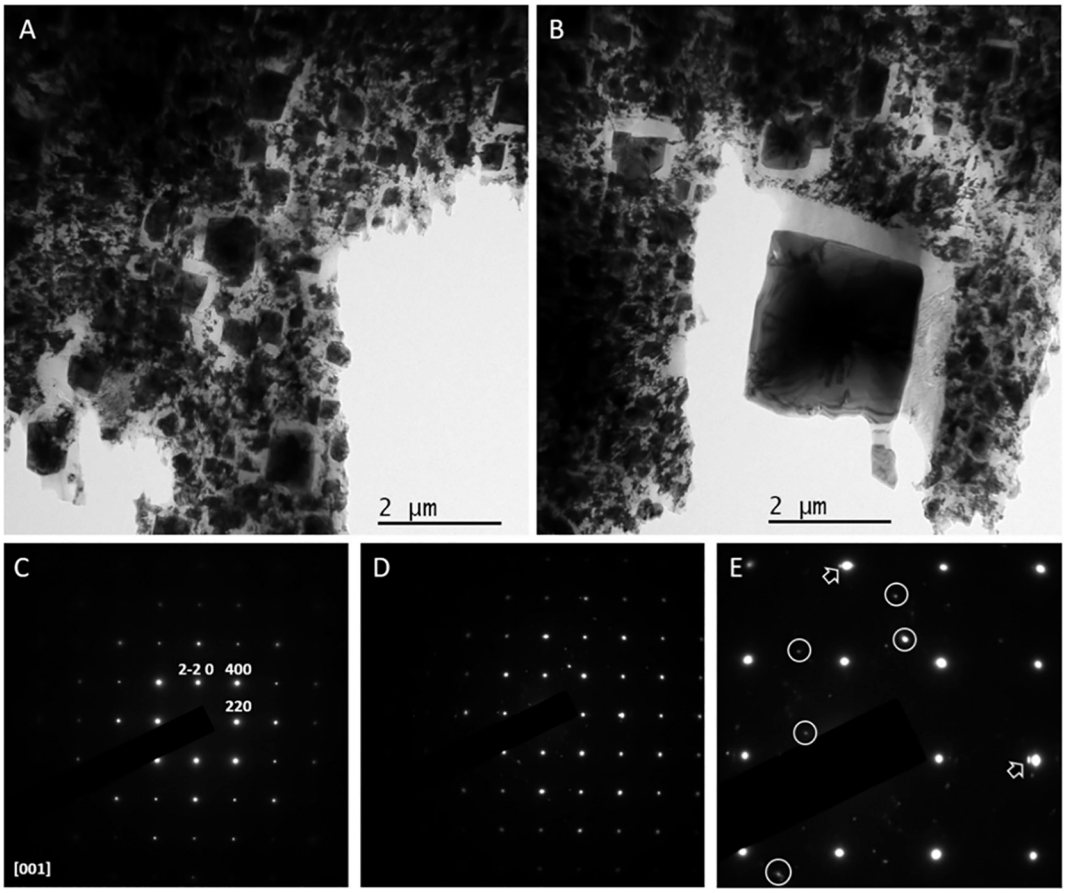

Fig. 5. (**A**) and (**B**) BF-TEM images showing several spinel crystals (dark grey), embedded within a layer-silicates envelope (bright grey). (**C**) Selected area electron diffraction (SAED) pattern relating to a single spinel crystal like that at the centre of fig. (B) oriented along [001]. Main diffraction spots indexed. (**D**) SAED pattern including several small dark crystals like those at the centre of fig. (A). (**E**) Enlargement of the central part of fig. (D). Note minor spot splitting (arrows) and some diffraction spots not pertinent to spinel but to the surrounding brighter phases (circles). These observations suggest a common orientation of all the spinel crystals, with minor mosaicity.

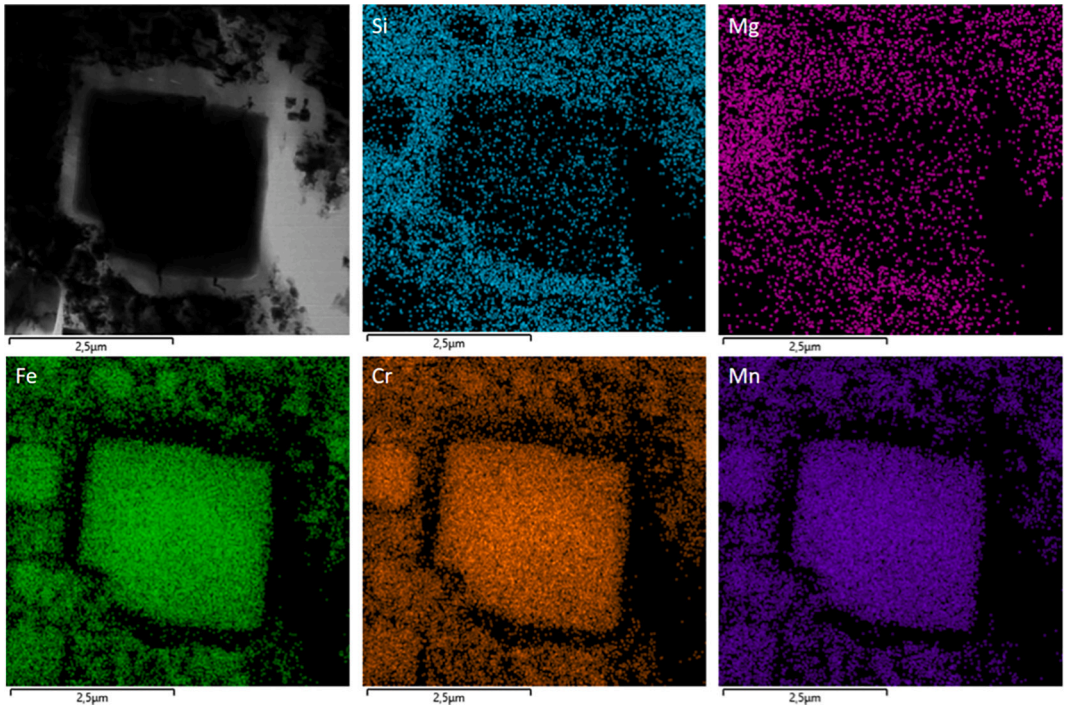

Fig. 6. BF-STEM image of spinel crystals (dark) and surrounding layer-silicates, together with EDS maps for Si, Mg, Fe, Cr and Mn. Note how Fe, Cr and Mn are correlated and outline spinel, whereas Si and Mg, correlated among them and uncorrelated with the former, outline Mg silicates surrounding spinel.

Table 4
TEM-EDS analyses of spinel recalculated on the base of three total cations.

a.p.f.u.	1	2	3	4	5	mean
Mg	0.05	0.04	0.04	0.05	0.04	0.04
Al	0.02	0.02	0.02	0.03	0.02	0.02
Si	0.03	0.03	0.03	0.04	0.05	0.04
Ca	0.01	0.02	0.00	0.02	0.02	0.01
Cr	1.10	1.08	1.15	1.11	1.07	1.10
Mn	0.53	0.53	0.48	0.50	0.50	0.51
Fe	1.25	1.25	1.25	1.23	1.29	1.25
Ni	0.01	0.02	0.01	0.02	0.01	0.01
Zn	0.01	0.01	0.01	0.01	0.00	0.01

Table 5
TEM-EDS analyses of layer-silicates recalculated to five cations.

a.p.f.u.	1	2	3	4	5	mean
Mg	2.50	2.41	2.37	2.26	2.28	2.36
Al	0.50	0.50	0.54	0.48	0.53	0.51
Si	1.54	1.55	1.63	1.55	1.71	1.60
Fe	0.09	0.10	0.11	0.10	0.10	0.10
Cr	0.35	0.43	0.35	0.60	0.36	0.42
Mn	0.02	0.01	0.00	0.02	0.02	0.01
Cl	0.07	0.07	0.13	0.15	0.21	0.13

Table 5 reports the average TEM-EDS compositions of layer-silicates. When recalculated to five cations, the final formula indicates an aluminous Mg layer-silicate, namely:

$(Mg_{2.36}Cr_{0.42}Fe_{0.10}Al_{0.10}Mn_{0.01})_{\Sigma=2.99}(Si_{1.59}Al_{0.41})_{\Sigma=2.00}O_{5.11}(OH_{3.87}Cl_{0.13})$

The layer-silicate, on the base of lattice fringe spacing on HRTEM images, was identified as a 7 Å phase (Fig. 7). Its chemical composition is compatible with an aluminous lizardite and it is characterized by not negligible Cr and Cl values. In any case, if it is indeed lizardite, its chemical composition significantly differs from those of the several lizardite generations analysed by SEM-EDS in the serpentinite matrix (Fig. 4 and Table 3).

The (001) planes of the layer-silicates have sharp contacts with, and are parallel to, the {111} planes of spinel, i.e., layer-silicates and spinel share planes of dense packed oxygens, suggesting local topotactical replacement of spinel by layer-silicates (Fig. 7). Either lattice fringe images and SAED patterns did not reveal any 14 Å phase (i.e., a normal 14 Å chlorite); only the sporadic presence of a rare 10 Å phase, possibly a mica-like phase, was noticed (Fig. 7B).

4. Discussion

Given the widespread occurrence of peridotites both on the ocean floor and in the allochthonous ophiolite complexes, the study of the serpentinization process has been the subject of many papers (e.g., Saumur and Hattori, 2013 with references therein). During serpentinization, mafic silicates are the first phases to alter releasing Si, Mg, and Fe, while the primary spinel releases Al, Fe, and Cr.

4.1. The serpentinization process

The preservation of microstructures of the harzburgite protolith indicates that serpentinization of "*Verde Prato*" has been a constant-volume process (e.g., Thayer, 1966). This implies a significant element removal (about 30 wt%) from the harzburgite to compensate for the influx of water (ca. 13 wt%) to make serpentine.

As evident from the phase map of Fig. 4, serpentinization has been a complex polyphase process. Based on geometric relationships among the different serpentine domains, at least eight serpentinization events have been identified, each one characterized by lizardites with different composition, especially as regards the Al and Fe contents (Fig. 4 and Table 3).

The relatively high Al-content of some lizardite generations (Tables 2 and 3) might be interpreted as either a submicroscopic intergrowth with a 14 Å-chlorite, or the result of a solid solution with amesite component (Nelson and Roy, 1958). Since the XRPD patterns of lizardite never showed the presence of the strong basal (001) peak characteristic of 14

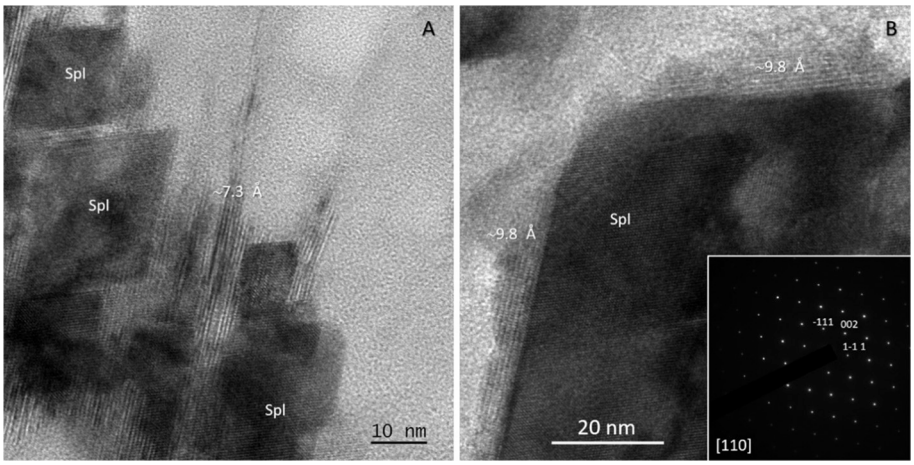

Fig. 7. HRTEM images of spinel crystals, as seen down [110], in contact with aluminous Mg layer-silicate. **A**) Rhomb-shaped (actually resulting from the projection of a tilted square) spinel crystals (dark) in contact with a 7 Å layer-silicate. **B**) Spinel crystal in contact with a 10 Å layer-silicate. Note how the (001) lattice fringes of both layer-silicates are parallel to the {111} planes of spinel, i.e., for both layer-silicates and spinel the planes of dense packed oxygens, suggesting local topotactical replacement of spinel by layer-silicates.

Å-chlorite (see appendix A), the serpentine must necessarily be an Al-rich lizardite.

The occurrence of Al-rich lizardite explains the absence of the 14 Å-chlorite corona that normally consumes the Al released from the hydrothermal alteration of the mantle spinel. Though the widespread occurrence of Al-lizardites appears difficult to reconcile with the general opinion that Al is a poorly mobile element, recent experiments by Andreani et al. (2013) and Pens et al. (2016), carried out at normal hydrothermal conditions ($P = 200$ MPa and $T = 200$–300 °C) in a saline (NaCl) hydrous fluid, indicate that Al speeds up the olivine dissolution and facilitates nucleation and growth of an Al-enriched lizardite.

The different lizardite generations formed in conjuction with a series of brittle tectonic events that opened fractures in the shallowest part of the mid-ocean ridge, favoring the influx of hydrothermal fluids. The wide compositional range of Al-lizardites suggests that during each serpentinization stage, also hydrothermal fluids had different compositions, especially with regards to Al and Fe.

The thermobaric conditions of the "*Verde Prato*" alteration can be constrained by the stability of lizardite and by the rheological behaviour of ultramafics, that suggest T lower than 350–400 °C, considered the upper boundary of lizardite stability field (Evans, 2004). However, most likely temperatures have been even lower than 300–350 °C, which has been experimentally demonstrated to be the thermal threshold above which lizardite begins to lose strength and to assume ductile behaviour (Raleigh and Paterson, 1965). Similar reasoning can be made for pressures too, since experiments did show that at these temperatures lizardite deforms brittlely only below 0.2 GPa (e.g., Escartín et al., 1997; Moore et al., 1997; Verlag and Byerlee, 1978).

4.2. The alteration of mantle spinel

Natural mantle Al-Cr-spinels have compositions close to the general formula $(Mg, Fe^{2+})(Cr, Al, Fe^{3+})_2O_4$ (Irvine, 1965), where Mn occurs only as a trace element. The relict "picotite" (*Spl1*) preserved in a few "*Verde Prato*" samples is in line with literature data.

The ubiquitous "normal" alteration of mantle spinel occurs in two stages (Eslami et al., 2023, and references therein). In the first stage, a Fe^{3+}-poor Cr-spinel (often referred to as *"ferrian"* Cr-spinel) forms, probably under reducing conditions and high silica activity, accompanied by the coeval growth of chlorite. In the second stage, referred to lower temperature hydrothermal oxidizing conditions, the *"ferrian"* Cr-spinel is enriched in Fe^{3+}. Therefore, during the ocean-floor serpentinization, the primary spinel composition evolves towards the chromite end-member ($FeCr_2O_4$) and/or towards "*ferrian"* Cr-spinel compositions, with $Cr^{3+} > Fe^{3+} > Al^{3+}$.

The "*ferrian"* Cr-spinel compositions, $(Fe^{2+}, Mg)Cr_2O_4$, with $Fe^{2+} >> Mg^{2+}$ and $Fe^{3+} >> Al^{3+}$, have been often described as "*ferritchromite*" (*Ferritchromit* in German), a term coined by Spangenberg (1943), as reported in Beeson and Jackson (1969) to refer to an "opaque substance, that according to chemical and physical properties, must lie between chromite and magnetite". "*Ferritchromite*" is usually surrounded by a chlorite aureole. The real nature of "*ferritchromite*" was revealed by a TEM study of Mellini et al. (2005) on hydrothermally altered mantle Al-spinels of Apennine serpentinized harzburgites of southern Tuscany (Italy): "*ferritchromite"* consists of a complex, nanometric association of Cr-magnetite, chlorite and lizardite, with $(001)_{Chl/Liz}$ always parallel to $(111)_{Cr\text{-}Mag}$.

The TEM results indicate that *Spl2* consists of a submicrometric aggregate of a 7 Å layer-silicate (Al-lizardite) and a secondary euhedral Mn-rich spinel that is a solid solution of manganochromite and Cr-magnetite. The systematic preferred orientation of the euhedral Mn-rich spinel suggests inheritance from an original single crystal of mantle spinel. This submicrometric intergrowth of layer-silicate and euhedral Mn-rich spinel is very similar to the microstructure described for the alteration of mantle Al-Cr spinels from Apenninic serpentinized harzburgites (e.g., Mellini et al., 2005). However, the Mn-rich spinel has composition quite different from the pure Cr-magnetite commonly reported in literature. A further difference concerns the lack in the "*Verde Prato*" of the 14 Å-chlorite corona surrounding the site of the former mantle spinel, that is interpreted as the reaction product of the Al released by the mantle spinel alteration with the surrounding ultramafite (Mellini et al., 2005).

Secondary spinels with significant Mn-content were also reported from alteration of mantle spinel, albeit in peculiar geological contexts. For example, in serpentinized harzburgites from the Northern Central Indian Ridge, Banerjee et al. (2015) describe two types of spinel alterations: a first type rich in FeO_{tot}, and a second type, where the original Al-spinel is replaced by "*ferritchromite*", typically enriched in Cr_2O_3, TiO_2 and MnO. In particular, the Mn-content is gradually decreasing from "*ferritchromite*" (MnO up to 8 wt%) to zero in the surrounding magnetite/Cr-magnetite.

Secondary spinels enriched in Mn were also reported by Fanlo et al. (2015) from some ore deposits of the Bou-Azzer mining district (Morocco), where ophiolite-related serpentinites include Co-Ni arsenide and Cu-rich sulphide deposits that contain disseminated Zn-, Mn- and Co-rich Cr-spinels, with MnO contents as high as 20 wt%.

The origin of Mn in the spinel alteration is not difficult to explain since serpentinization occurred on the ocean floor, where Fe-Mn nodule deposits are widespread (e.g., Hein et al., 1997). However, the primary origin of these elements is to be found in correspondence with hydrothermal vents that occur in the proximity of spreading centres along mid-ocean ridges, especially in correspondence with transform faults. Therefore, it is reasonable to assume that the mantle spinel of "*Verde Prato*" was altered by a metasomatizing fluid enriched in Mn coming from the proximity of a hydrothermal vent. The contribution of seawater is further supported by the presence of Cl isomorphically replacing OH-groups in the layer-silicates intergrown with manganochromite, as already documented by Anselmi et al. (2000) in a chemical and mineralogical study of lizardite-serpentinites from Elba, Monti Livornesi and Murlo ophiolites.

5. Conclusions

Unlike other ophiolitic mantle ultramafics, where mineralogy and structure have been completely reset in the spinel-peridotite facies, the "*Verde Prato*" serpentinite locally preserves microstructures recalling part of the previous history. Such microstructures, consisting of corroded shards of an opaque phase (*Spl2*) surrounded by clear lizardite (e.g., Fig. 2), are considered to represent a former mantle spinel + orthopyroxene intergrowth, i.e., the breakdown products of former garnet during decompression from the garnet-peridotite to the spinel-peridotite facies conditions.

SEM-EDS analyses of the opaque spinel *Spl2* systematically gave compositions with unusually high SiO_2 (≈ 17–18 wt%) and MnO (≈ 8–9 wt%) contents, that other microanalytical techniques, such as μ-Raman and μ-XRPD, were unable to explain. Only TEM images showed that *Spl2* consists of a submicroscopic intergrowth of euhedral spinels with orthogonal contours, and layer-silicates, the latter slightly modally prevailing over the former.

Euhedral spinel crystals, which are Mn-rich (Mn-chromite–Cr-magnetite solid solution), share common orientation, suggesting inheritance from a former single crystal of the original mantle spinel.

The alteration of the *Spl2* exhibits a TEM microstructure similar to that described for other Apenninic serpentinites by Mellini et al. (2005). However, in the latter case, the final product is a Cr-magnetite and a 14 Å-chlorite occurs among the alteration products, forming a corona around the mantle spinel site.

A detailed study of the serpentinite matrix identified at least eight different hydration stages (Fig. 4), characterized by lizardites of different compositions, systematically enriched in Al and Fe. The high Al content indicates a significant amesite component in lizardite and explains the lack of the chlorite corona around the mantle spinel site. The formation of Al-rich lizardite, that implies a greater Al-mobility during alteration of mantle spinel, has been recently supported by experimental studies of Pens et al. (2016).

The hydrothermal alteration of "*Verde Prato*" must have occurred on the floor of the Mesozoic Tethys Ocean (e.g., Mével, 2003), in proximity of a Mn-rich hydrothermal vent. Since the "*Verde Prato*" is lacking evidence of pervasive ductile deformation, it can be envisaged that the entire polyphase serpentinization process occurred at temperatures not higher than 300 °C and at $P < 0.2$ GPa, the two boundaries that constrain the brittle rheological behaviour of the lizardite serpentinite. It is, therefore, possible that the Al-lizardite is a serpentine mineral forming at the lowest T range of the lizardite stability. Only targeted research will be able to confirm this in the future.

CRediT authorship contribution statement

Giancarlo Capitani: Conceptualization, Investigation, Writing, Resources. **Roberto Compagnoni:** Conceptualization, Investigation, Writing – original draft. **Roberto Cossio:** Conceptualization, Investigation, Resources. **Linda Pastero:** Investigation. **Roberto Conconi:** Investigation. **Marcello Mellini:** Writing – original draft.

Declaration of competing interest

The authors declare that they have no known competing financial interests or personal relationships that could have appeared to influence the work reported in this paper.

Acknowledgements

The micro-Raman data were obtained with the equipment acquired by the 'G. Scansetti' Interdepartmental Center for Studies on Asbestos and Other Toxic Particulates through a grant of Compagnia di San Paolo, Torino. The Platform of Microscopy of Milano Bicocca has been co-funded by MIUR – Dipartimenti di Eccellenza 2023–2027, Project TECLA, and 2018–2022, Project Climate Change, Department of Earth and Environmental Sciences, University of Milano-Bicocca. The careful and constructive revisions of Fernando Nieto and an anonymous referee are greatly appreciated.

Appendix A. Supplementary data

Supplementary data to this article can be found online at https://doi.org/10.1016/j.lithos.2024.107777.

References

Andreani, M., Daniel, I., Pollet-Villard, M., 2013. Aluminum speeds up the hydrothermal alteration of olivine. Am. Mineral. 98, 1738–1744.
Anselmi, B., Mellini, M., Viti, C., 2000. Chlorine in the Elba, Monti Livornesi and Murlo serpentinites: evidence for sea-water interaction. Eur. J. Mineral. 12, 137–146.
Banerjee, R., Ray, D.H., Ishii, T., 2015. Mineral chemistry and alteration characteristics of spinel in serpentinised peridotites from the northern central Indian Ridge. J. Geol. Soc. India 86, 41–51. https://doi.org/10.1007/s12594-015-0279-3.
Barnes, S.T., Roeder, P.L., 2001. The range of spinel compositions in terrestrial mafic and ultramafic rocks. J. Petrol. 42 (12), 2279–2302. https://doi.org/10.1093/petrology/42.12.2279.
Bédard, É., Hébert, R., Guilmette, C., Lesage, G., Wang, C.S., Dostal, J., 2009. Petrology and geochemistry of the Saga and Sangsang ophiolitic massifs, Yarlung Zangbo suture zone, Southern Tibet: evidence for an arc-back-arc origin. Lithos 113, 48–67. https://doi.org/10.1016/j.lithos.2009.01.011.
Beeson, M.H., Jackson, E.D., 1969. Chemical composition of altered chromites from the Stillwater complex, Montana. Am. Mineral. 51, 1084–1100.
Bosi, F., Biagioni, C., Pasero, M., 2019. Nomenclature and classification of the spinel supergroup. Eur. J. Mineral. 31, 183–192. https://doi.org/10.1127/ejm/2019/0031-2788.
CARG, 2012. Cartografia Geologica Regione Toscana, continuum geologico in scala 1: 10,000. Regione Toscana. http://www.lamma.rete.toscana.it/carta-geologica-1-10000.
Coli, M., Compagnoni, R., Cossio, R., Del Ventisette, C., Vannucchi, P., 2023. The Monteferrato serpentinized peridotite (Figline di Prato, Prato) in the northern Apennines, Italy: a witness of the Ligurian Ocean margin in the monumental religious buildings of Tuscany. Ofioliti 48 (2), 105–120. https://doi.org/10.4454/ofioliti.v48i2.564105.
Conconi, R., Ventruti, G., Nieto, F., Capitani, G., 2023. TEM-EDS microanalysis: Comparison among the standardless, Cliff & Lorimer and absorption correction quantification methods. Ultramicroscopy 254, 113845. https://doi.org/10.1016/j.ultramic.2023.113845.
Escartín, J., Hirth, G., Evans, B., 1997. Non-dilatant brittle deformation of serpentinites: Implications for Mohr-Coulomb theory and the strength of faults. J. Geophys. Res. 102, 2897–2913. https://doi.org/10.1029/96JB02792.
Eslami, A., Malvoisin, B., Brunet, F., 2023. Hydrothermal alteration of chromitite-dunite pairs from the Sabzevar ophiolite (NE Iran): Chemical and nano-textural evolution of Cr-spinel. Lithos 442-443, 107093. https://doi.org/10.1016/j.lithos.2023.107093.
Evans, B.W., 2004. The Serpentinite Multisystem Revisited: Chrysotile is Metastable. Int. Geol. Rev. 46, 479–506. https://doi.org/10.2747/0020-6814.46.6.479.
Fanlo, I., Gervilla, F., Colás, V., Subías, I., 2015. Zn-, Mn- and Co-rich chromian spinels from the Bou-Azzer mining district (Morocco): Constraints on their relationship with the mineralizing process. Ore Geol. Rev. 71, 82–98. https://doi.org/10.1016/j.oregeorev.2015.05.006.
Guarnieri, L., Nakamura, E., Piccardo, G.B., Sakaguchi, C., Shimizu, N., Vannucci, R., Zanetti, A., 2012. Petrology, trace elements and Sr, Nd, Hf isotope geochemistry of the North Lanzo Peridotite Massif (Western Alps, Italy). J. Petrol. 52 (11), 2259–2306. https://doi.org/10.1093/petrology/egs049.

Hein, J.R., Koschinsky, A., Halbach, P., Manheim, F.T., Bau, M., Kang, J.K., Lubick, N., 1997. Iron and manganese oxide mineralization in the Pacific. In: Nicholson, K., Hein, J.R., Bfihn, B., Dasgupta, S. (Eds.), Manganese Mineralization: Geochemistry and Mineralogy of Terrestrial and Marine Deposits, Geological Society Special Publication, vol. 119, pp. 123–138. https://doi.org/10.1144/GSL.SP.1997.119.01.09.

Hellebrand, E., Snow, J.E., Dick, H.J.B., Hofmann, A.W., 2001. Coupled major and trace elements as indicators of the extent of melting in mid-ocean-ridge peridotites. Nature 410, 677–681. https://doi.org/10.1038/35070546.

Irvine, T.N., 1965. Chromian spinel as a petrogenetic indicator: part 1. Theory. Can. J. Earth Sci. 2 (6), 648–672. https://doi.org/10.1139/e65-046.

Lanari, P., O., De Andrade, V., Dubacq, B., Lewin, E., Eugene, G., Grosch, E.G., Schwartz, S., 2014. XMapTools: a MATLAB©-based program for electron microprobe X-ray image processing and geothermobarometry. Comput. Geosci. 62, 227–240. doi:https://doi.org/10.1016/j.cageo.2013.08.010.

Mellini, M., Rumori, C., Viti, C., 2005. Hydrothermally reset magmatic spinels in retrograde serpentinites: formation of “ferritchromit” rims and chlorite aureoles. Contrib. Mineral. Petrol. 149, 266–275. https://doi.org/10.1007/s00410-005-0654-y.

Mével, C., 2003. Serpentinization of abyssal peridotites at mid-ocean ridges. Compt. Rendus Geosci. 335, 825–852. https://doi.org/10.1016/j.crte.2003.08.006.

Moore, D.E., Lockner, D.A., Ma, S., Summers, R., Byerlee, J.D., 1997. Strengths of serpentinite gouges at elevated temperatures. J. Geophys. Res. Solid Earth 102, 14, 787–14,801. https://doi.org/10.1029/97JB00995.

Nelson, B.W., Roy, R., 1958. Synthesis of the chlorites and their structural and chemical constitution. Am. Mineral. 42, 707–725.

O'Neill, H.S.C., 1981. The transition between Spinel Lherzolite and Garnet Lherzolite, and its use as a Geobarometer. Contrib. Mineral. Petrol. 77, 185–194. https://doi.org/10.1007/BF00636522.

Pens, M., Andréani, M., Daniel, I., Perrillat, J., Cardon, H., 2016. Contrasted effect of aluminum on the serpentinization rate of olivine and orthopyroxene under hydrothermal conditions. Chem. Geol. 441, 256–264. https://doi.org/10.1016/j.chemgeo.2016.08.007.

Raleigh, C., Paterson, M.S., 1965. Experimental deformation of serpentinite and its tectonic implications. J. Geophys. Res. 70, 3965–3985. https://doi.org/10.1029/JZ070i016p03965.

Saumur, B.M., Hattori, K., 2013. Zoned Cr-spinel and ferritchromite alteration in forearc mantle serpentinites of the Rio San Juan complex, Dominican Republic. Mineral. Mag. 77 (1), 117–136. https://doi.org/10.1180/minmag.2013.077.1.11.

Shimizu, Y., Arai, S., Morishita, T., Ishida, Y., 2008. Origin and significance of spinel-pyroxene symplectite in lherzolite xenoliths from Tallante, SE Spain. Mineral. Petrol. 94, 27–43. https://doi.org/10.1007/s00710-008-0004-7.

Spangenberg, K., 1943. Die Chromitlagerstätte vom Tampadel in Zobten. Zeitschr. prakt. Geologie 51, 13–35.

Thayer, T.P., 1966. Serpentinization considered as a constant-volume metasomatic process. Am. Mineral. 51, 685–710.

Verlag, B., Byerlee, J.D.D., 1978. Friction of rocks. Pure Appl. Geophys. 116, 615–626.